



# Simulation and analysis of stress in a Li-ion battery with a blended $\text{LiMn}_2\text{O}_4$ and $\text{LiNi}_{0.8}\text{Co}_{0.15}\text{Al}_{0.05}\text{O}_2$ cathode



Yiling Dai, Long Cai, Ralph E. White\*

Department of Chemical Engineering, University of South Carolina, Columbia, SC 29208, USA

## HIGHLIGHTS

- A model is developed to simulate the stress generated in a blended cathode.
- The effect of the blend ratio on the stress generation is investigated.
- It shows that the fracture potentially occurs in the particles near the separator.
- The stress in the LMO is reduced at the end of discharge due to adding the NCA.

## ARTICLE INFO

### Article history:

Received 13 May 2013

Received in revised form

26 August 2013

Accepted 27 August 2013

Available online 4 September 2013

### Keywords:

Lithium ion battery

Stress

Model

Multiple active materials

LMO

NCA

## ABSTRACT

Stress generation due to Li ion insertion into/extraction from  $\text{LiMn}_2\text{O}_4$  particles is studied with a mathematical model for a lithium ion battery with pure  $\text{LiMn}_2\text{O}_4$  or mixed  $\text{LiMn}_2\text{O}_4$  and  $\text{LiNi}_{0.8}\text{Co}_{0.15}\text{Al}_{0.05}\text{O}_2$  cathode. The simulated stress profile in a pure  $\text{LiMn}_2\text{O}_4$  electrode shows nonuniformity across the positive electrode. The cathode blended model predicts that the stress generated in the  $\text{LiMn}_2\text{O}_4$  particles is reduced at the end of discharge due to adding  $\text{LiNi}_{0.8}\text{Co}_{0.15}\text{Al}_{0.05}\text{O}_2$  to the cathode. The effect of the variation in the blend ratio on the stress generation is also investigated.

© 2013 Elsevier B.V. All rights reserved.

## 1. Introduction

Spinel  $\text{LiMn}_2\text{O}_4$  (LMO) is one of the most attractive positive electrodes for high power applications such as hybrid/plug-in hybrid electrical vehicles (HEV/PHEVs). It shows great benefits in the area of cost, safety and power density, which are major concerns of large format applications in the automotive industry. However, this spinel material exhibits serious capacity fade during cycling or storage at elevated temperature which makes it less competitive with other cathode materials [1]. Recent studies have revealed that capacity fade in spinel LMO cathodes is mostly due to manganese (Mn) dissolution and its toxic effect on the carbon anode [2–4]. There are at least two possible reasons for the Mn dissolution: (1) acid attack and a disproportionation reaction of

Mn(III) on the particle surface [5–7]; (2) the instability of the two-phase structure in the charged state which leads to the loss of MnO and the dissolution of Mn(II) to form a more stable single-phase structure [8].

Several improvements have been made to increase the long term stability of the LMO based cells by using surface treatment or element substitution. For example, Amatucci et al. [9] have investigated the effects of modifying the surface of LMO on the cell performance at high temperatures. The surface improvement helps to reduce Mn dissolution and retain capacity. Doped spinel  $\text{LiMn}_{2-x}\text{M}_x\text{O}_4$  (where M = Li, Co, Cr, Ni etc.) materials have also been reported to be effective for the improvement of the cell high temperature performance [10–13]. The benefit of doping elements in LMO has been attributed to the stabilization of the spinel structure. Among them, the doped material with lithium substitution of Mn sites has higher theoretical capacity than others because of the light element lithium, but the doped material retain the native low capacity of LMO. In order to increase the reversible

\* Corresponding author. Tel.: +1 803 7773270; fax: +1 803 7778265.  
E-mail address: [white@cec.sc.edu](mailto:white@cec.sc.edu) (R.E. White).

capacity after the cation doping while keeping the other electrochemical performance,  $F^-$  ions were introduced in place of  $O^{2-}$  ions [14,15]. Unfortunately, the cost for the production of the doped materials is significantly high.

A promising approach was first provided by Numata et al. to improve the capacity retention for LMO based electrodes by adding  $LiNi_{0.8}Co_{0.2}O_2$  [16]. They found that both the Mn dissolution from the LMO and the acid generation decreased with the addition of  $LiNi_{0.8}Co_{0.2}O_2$ . Myung et al. [17] investigated the behavior of the electrode with the LMO and  $LiNi_{0.8}Co_{0.15}Al_{0.05}O_2$  (NCA) mixture. They found that a cell with the mixed electrode had better cycle performance at elevated temperature than a cell with a pure LMO electrode. In addition, the capacity of the LMO based electrode has been enhanced by adding high capacity NCA. Recently, Tran et al. [18] reported on the electrochemical and thermal behavior of LMO and NCA blended electrodes. Their results indicated that the NCA addition increased the capacity of blends and reduced the Mn dissolution from the spinel, but harmed the rate capacity; On the other hand, with the existence of LMO the heat generation from the blends is less than that from the pure NCA. According to their study, blends with 33.3 wt% NCA have the best behavior. Manthiram et al. [19] studied the suppression of the Mn dissolution in spinel cathodes by mixing LMO or its doping derivatives with layered oxide cathodes such as:  $LiCoO_2$  and  $LiNi_{0.85}Co_{0.15}O_2$ . They observed that  $LiCoO_2$  was more effective than  $LiNi_{0.85}Co_{0.15}O_2$  in improving the storage and cycle performance of LMO based electrodes. Smith et al. [20] showed that the addition of  $Li[Ni_{1/3}Mn_{1/3}Co_{1/3}]O_2$  to the LMO electrode produced a great improvement in the capacity retention. Also, it was found that the  $Li[Ni_{1/3}Mn_{1/3}Co_{1/3}]O_2$  helped to reduce the Mn dissolution from the LMO electrode. Now, Li-ion batteries with LMO mixed with other insertion active material as cathodes have been commercialized such as Samsung SDI Li-ion batteries.

The mechanical degradation under cycling is one of the most important failure mechanisms of modern Li-ion batteries. It has been reported that the fractures and cracks exist in several electrode materials after Li insertion/extraction [21–24]. For example, Lim et al. [23] have observed an evident disruption in the LMO particle after electrochemical cycling. There is about 6.5% volume change when the LMO is lithiated from empty state to full state [25]. However, the particle volume change inside particle is not uniform. This gives rise to stress and produces cracks or fractures in the particle. Furthermore, the particle fracture will generate fresh active material surface on which the new solid electrolyte interface (SEI) film is formed. In the meanwhile, the particle fracture can also lead to loss of connection of the active material particle to the conductor [26].

Mathematical models have been largely applied to investigate the stress generation and the effect of stress on battery degradation. Christensen et al. [27,28] developed an integrated model based on the theories of transport and elasticity to simulate the stress inside active material particles. Zhang et al. [29] studied the intercalation-induced stress in LMO particles by considering the intercalation-induced stress as being analogous to thermal stress. Their approach showed similar results to those of Christensen et al. Without considering the stress-driven diffusion in Zhang et al.'s approach, Cheng et al. [30] obtained an analytical solution for the generation of stress in a spherical particle under galvanostatic and potentiostatic operation.

Unlike the studies above on single particles only, there are several papers on the stress generation in a porous composite electrode. Garcia et al. [31] developed a two-dimensional model with particle distribution to compute stress in the porous electrode. Also, their model account for the potential and Li-ion concentration distribution in the solution. However, their model is very computationally intensive and the stress-driven diffusion has been

ignored. Golmon et al. [32] combined the mechanical equation and porous electrode theory (the pseudo two dimensional (P2D) model) together to investigate the stress distribution in porous electrode. They applied homogenization techniques to relate the parameters between the micro-scale and the macro-scale. Similarly, Renganathan et al. [33] studied the stress generation in a  $LiCoO_2$ /Carbon battery including the phase change in the  $LiCoO_2$ . Christensen [34] simulated the stress generation in a porous electrode by incorporated the model for stress generation in single particle [27,28] to the P2D model. Recently, Bower et al. [35] proposed a finite-strain elastic-plastic model to predict the variation of stress and electric potential in a one-dimensional half-cell.

However, the stress generation in an electrode with multiple active materials has not been published in the open literature. To obtain a better understanding of the properties of Li-ion batteries with blended material cathodes, we present a theoretical study of the mechanical behavior of electrodes made from mixing LMO and NCA. The mechanical equations capturing the stress generation in the spherical particles in the electrodes are incorporated into the classical P2D model. To elucidate the effect of mixing, simulations are conducted and compared for both pure LMO electrodes and blended electrodes with LMO and NCA. Simulation results for a mixed electrode show that the stress generated in the LMO particles is significantly reduced at the end of discharge due to adding NCA to the electrode. This stress reduction might partially explain why experimental investigations show that the performance of the LMO based electrodes can be improved by adding NCA. We also investigated the mixing ratio on the stress generation of the blended electrode. Simulations for mixed electrodes with different blend ratios show that the reduced stress region increases by increasing the NCA ratio.

## 2. Model development

In this study, we have combined P2D model and mechanical equations to study the stress generated due to Li insertion into/extraction from the active material particles in a lithium ion battery. This approach is similar to Renganathan et al.'s work to study the  $LiCoO_2$ /Carbon battery [33], but we have extended their work to electrodes with multiple active materials in the cathode. Furthermore, because no phase change is considered during Li insertion into/extraction from the active material particles, we could express the stress profile as function of concentration. To obtain the stress profile in the P2D model, we modified the diffusion equation in the classic P2D model, which is shown in detail below.

The Li-ion battery considered in this study consists of three regions: a positive electrode (pure LMO or LMO mixed with NCA), a separator, and a carbon negative electrode as shown in Fig. 1. For an electrode that has more than one active material, it is assumed that the materials in the electrode are well mixed and their properties (such as: diffusion coefficients, reaction rate constants and so on) remain the same as those in a pure material electrode. The parameters for the mixed positive electrode used in this model were obtained from the work by Albertus et al. [36], in which the electrochemical behavior of a mixed cathode half-cell was simulated. In the following, we will briefly introduce the mechanical equations and the porous electrode model equations.

### 2.1. Mechanical stress model

In this work, the stress generated due to Li-ion intercalation/deintercalation process is calculated using an approach similar to that due to volumetric thermal expansion. The thermal stress analysis of an isotropic media can be described by Hooke's law with additional thermal expansion term [37]:

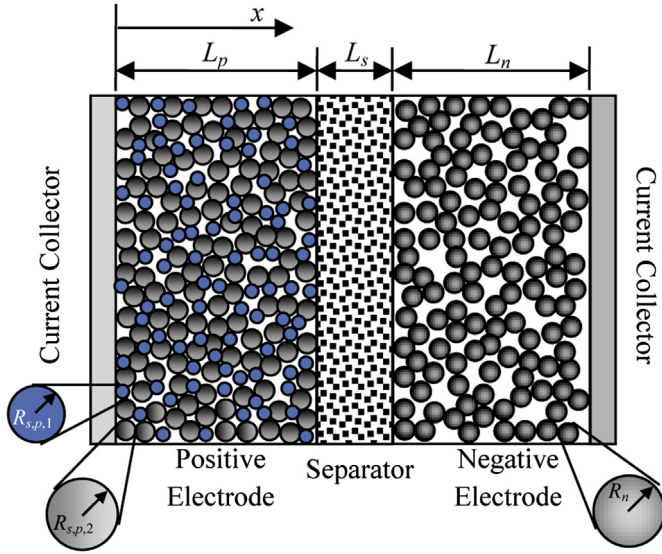


Fig. 1. Schematic of a Li-ion battery.

$$\varepsilon_{ij} = \frac{1}{E} [(1+\nu)\sigma_{ij} - \nu\sigma_{kk}\delta_{ij}] + \alpha\Delta T\delta_{ij} \quad (1)$$

where  $\varepsilon_{ij}$  and  $\sigma_{ij}$  represent the strain and stress tensor components, respectively;  $E$  is Young's modulus,  $\nu$  is Poisson's ratio,  $\delta_{ij}$  is Kronecker delta,  $\alpha$  is the thermal expansion coefficient, and  $\Delta T$  represents the temperature difference from the original value.

Analogously, in the case of small deformation, a stress–strain relationship including a concentration diffusion in an isotropic media can be represented as [38]:

$$\varepsilon_{ij} = \frac{1}{E} [(1+\nu)\sigma_{ij} - \nu\sigma_{kk}\delta_{ij}] + \frac{\Delta c_s \Omega}{3} \delta_{ij} \quad (2)$$

where  $\Omega$  is the partial molar volume,  $\Delta c_s = c_s - c_s^0$  is the concentration change of the diffusing species from original value,  $c_s^0$  and  $c_s$  is the concentration of the diffusing species.

For a spherical particle, there are only two independent components in the stress tensor: the radial component ( $\sigma_r$ ) and the tangential component ( $\sigma_t$ ). Therefore, the equilibrium condition for the stress tensor in a particle is simplified as follows [29]:

$$\frac{d\sigma_r}{dr} + \frac{2}{r}(\sigma_r - \sigma_t) = 0 \quad (3)$$

Also, strain–stress relations can be written according to equation for a spherical particle [29],

$$\begin{aligned} \varepsilon_r &= \frac{1}{E} (\sigma_r - 2\nu\sigma_t) + \frac{\Omega}{3}\Delta c_s \\ \varepsilon_t &= \frac{1}{E} [\sigma_t - \nu(\sigma_t + \sigma_r)] + \frac{\Omega}{3}\Delta c_s \end{aligned} \quad (4)$$

The stresses can be written as a function of strains

$$\begin{aligned} \sigma_r &= \frac{E}{(1+\nu)(1-2\nu)} \left[ (1-\nu)\varepsilon_r + 2\nu\varepsilon_t - (1+\nu)\frac{\Delta c_s \Omega}{3} \right] \\ \sigma_t &= \frac{E}{(1+\nu)(1-2\nu)} \left[ \nu\varepsilon_r + \varepsilon_t - (1+\nu)\frac{\Delta c_s \Omega}{3} \right] \end{aligned} \quad (5)$$

Also, strains can be related to the displacement  $u$  in a spherical particle as follows:

$$\begin{aligned} \varepsilon_r &= \frac{du}{dr} \\ \varepsilon_t &= \frac{u}{r} \end{aligned} \quad (6)$$

The  $u$  is defined as the difference between the radial position of a lattice at time  $t$ , and the initial radial position of that lattice element.

By substituting Eq. (6) into (5), the stress tensor can be expressed in terms of displacement  $u$  as follows:

$$\begin{aligned} \sigma_r &= \frac{E}{(1+\nu)(1-2\nu)} \left[ (1-\nu)\frac{du}{dr} + 2\nu\frac{u}{r} - (1+\nu)\frac{\Delta c_s \Omega}{3} \right] \\ \sigma_t &= \frac{E}{(1+\nu)(1-2\nu)} \left[ \nu\frac{du}{dr} + \frac{u}{r} - (1+\nu)\frac{\Delta c_s \Omega}{3} \right] \end{aligned} \quad (7)$$

Substitute Eq. (7) into the equilibrium condition (Eq. (3)) yields the displacement equation which is shown as following:

$$\frac{d^2u}{dr^2} + \frac{2}{r}\frac{du}{dr} - \frac{2u}{r^2} = \frac{1+\nu}{1-\nu}\frac{\Omega}{3}\frac{dc_s}{dr} \quad (8)$$

Integrating Eq. (8) yields:

$$\frac{du}{dr} + 2\frac{u}{r} = \frac{1+\nu}{1-\nu}\frac{\Omega}{3}c + Z_1 \quad (9)$$

Integrating Eq. (9) yields:

$$u = \frac{1}{r^2} \left( \int \frac{1+\nu}{1-\nu}\frac{\Omega}{3}c_s r^2 dr + \frac{Z_1 r^3}{3} + Z_2 \right) \quad (10)$$

where  $Z_1$  and  $Z_2$  are integration constants. These two constants can be obtained from the two boundary conditions: the radial stress is zero on the particle surface ( $r = R_0$ )

$$\sigma_r|_{(r=R_0)} = 0 \quad (11)$$

and the stress remains finite at the particle center ( $r = 0$ ), that is:

$$\left. \frac{d\sigma_r}{dr} \right|_{(r=0)} = 0 \quad (12)$$

Substituting the solution for  $u$  into Eq. (7), results in the following expressions for the two stress components [29]:

$$\begin{aligned} \sigma_r &= \frac{2QE}{3(1-\nu)} \left[ \frac{1}{R_0^3} \int_0^{R_0} c_s r^2 dr - \frac{1}{r^3} \int_0^r c_s \zeta^2 d\zeta \right] \\ \sigma_t &= \frac{QE}{3(1-\nu)} \left[ \frac{2}{R_0^3} \int_0^{R_0} c_s r^2 dr + \frac{1}{r^3} \int_0^r c_s \zeta^2 d\zeta - c_s \right] \end{aligned} \quad (13)$$

where  $\zeta$  is a dummy integration variable.

Finally, the hydrostatic stress,  $\sigma_h$ , is defined and given as follows [29,38]:

$$\sigma_h = \frac{\sigma_r + 2\sigma_t}{3} = \frac{2QE}{9(1-\nu)} \left( \frac{3}{R_0^3} \int_0^{R_0} c_s r^2 dr - c_s \right) \quad (14)$$

Because the Eqs. (13) and (14) are derived without assuming that there is constant applied current/flux on the particle surface, it is reasonable to combined this with the P2D model as shown below.

## 2.2. Porous electrode model

The porous electrode model (P2D model) has been applied to simulate the behavior of Li-ion batteries in many literature [39–41]. The mass balance and the charge balance are considered in the both solution phase and the solid phase. We only briefly introduce the

model here as follows. A detailed explanation of the porous electrode models can be found elsewhere [39–41].

The mass balance for  $\text{Li}^+$  in the electrolyte is given as follows:

$$\varepsilon_{2,j} \frac{\partial c_{\text{Li}^+}}{\partial t} = -\nabla \cdot \left( -D_{\text{eff,Li}^+,j} \nabla c_{\text{Li}^+} \right) + \frac{1-t^+}{F} I_j, \quad j = p, s, n \quad (15)$$

where  $\varepsilon_{2,j}$  is the porosity in cell component  $j$  ( $j = p$  for the cathode,  $j = s$  for the separator, and  $j = n$  for the anode),  $c_{\text{Li}^+}$  is the concentration of  $\text{Li}^+$ ,  $D_{\text{eff,Li}^+,j}$  is the effective diffusivity of  $\text{Li}^+$  in the electrolyte,  $t^+$  is the transport number of  $\text{Li}^+$ ,  $F$  is Faraday's constant, and  $I_j$  is the local total current density ( $\text{A m}^{-3}$ ). The potential in the solid phase,  $\phi_1$ , is given by Ohm's law as follows:

$$\nabla \cdot \left( -\sigma_{\text{eff},j} \nabla \phi_1 \right) = -I_j, \quad j = p, n \quad (16)$$

where  $\sigma_{\text{eff},j}$  is the effective conductivity in the solid phase.

The solution phase potential,  $\phi_2$ , is given by:

$$\nabla \cdot \left( \kappa_{\text{eff},j} \nabla \phi_2 - 2 \frac{\kappa_{\text{eff},j} RT (1-t^+)}{F} \left( 1 + \frac{\partial \ln f}{\partial \ln c_{\text{Li}^+}} \right) \nabla \ln c_{\text{Li}^+} \right) = I_j, \quad j = p, s, n \quad (17)$$

where  $\kappa_{\text{eff},j}$  is the effective conductivity in the solution phase,  $R$  is the gas constant,  $T$  is the temperature,  $f$  is the ionic activity coefficient.

The local total current density,  $I_j$ , is the sum of current densities for all types of particles

$$I_j = \sum_k^{k_j} a_{k,j} i_{k,j}, \quad j = p, n \quad (18)$$

where  $k_j$  is particle types in region  $j$ . In the positive electrode, there are two types of particles: LMO and NCA; in the negative electrode, there is only one particle type.  $a_{k,j}$  is the specific surface area of type particle  $k$  and is defined as

$$a_{k,j} = \frac{3\varepsilon_{1,k,j}}{R_{s,k,j}} \quad (19)$$

where  $\varepsilon_{1,k,j}$  is the volume fraction of the particles type  $k$  in region  $j$ , and  $R_{s,k,j}$  is the radius of the particle type  $k$ .  $i_{k,j}$  is the local transfer current for the particles type  $k$  and is described by the Butler–Volmer expression as follows:

$$i_{k,j} = i_{0,k,j} \left[ \exp \left( \frac{\alpha_{a,\text{Li}} F}{RT} \eta_{k,j} \right) - \exp \left( -\frac{\alpha_{c,\text{Li}} F}{RT} \eta_{k,j} \right) \right] \quad (20)$$

where  $i_{0,k,j}$  is the exchange current density for particles type  $k$  in region  $j$  and is defined as:

$$i_{0,k,j} = F k_{\text{Li},k,j} c_{\text{surf},k,j}^{0.5} (c_{\text{max},k,j} - c_{\text{surf},k,j})^{0.5} c_{\text{Li}^+}^{0.5} \quad (21)$$

where  $k_{\text{Li},k,j}$  is the reaction rate constant for the particles type  $k$ ,  $c_{\text{surf},k,j}$  is the surface concentration of  $\text{Li}^+$  for the particles type  $k$ ,  $c_{\text{max},k,j}$  is the maximum concentration of  $\text{Li}^+$  in the particles type  $k$ . The over-potential for particle type  $k$  in region  $j$  is given by:

$$\eta_{k,j} = \phi_1 - \phi_2 - U_{k,j} - i_{k,j} R_{\text{conc},k,j} \quad (22)$$

where  $U_{k,j}$  is open circuit potential for particle type  $k$  in region  $j$ ,  $R_{\text{conc},k,j}$  is the contact resistance between the bulk conductor and

the surface of particle type  $k$ . The effective properties are discussed and presented in the [Appendix](#).

### 2.3. Diffusion in the solid phase

The diffusion equation is modified by including the stress-driven diffusion. The pore wall flux,  $J_k$ , for particles type  $k$  including the stress-driven diffusion can be expressed as following [29,38]:

$$J_k = -D_{s,k} \left( \nabla c_{s,k} - \frac{\Omega c_{s,k}}{RT} \nabla \sigma_{h,k} \right) \quad (23)$$

where  $D_{s,k}$  is the diffusion coefficient in particles type  $k$ ,  $c_{s,k}$  is Li ion concentration in particles type  $k$ , and  $\sigma_{h,k}$  is the hydrostatic stress of particle  $k$ . The mass balance for Li ions in particles type  $k$  is given by:

$$\frac{\partial c_{s,k}}{\partial t} = -\nabla \cdot J_k \quad (24)$$

with two boundary conditions as following:

$$\begin{aligned} J_k|_{(r=0)} &= 0 \\ J_k|_{(r=R_{0,k})} &= \frac{i_k}{F} \end{aligned} \quad (25)$$

Substitute Eqs. (23) into (24),

$$\frac{\partial c_{s,k}}{\partial t} = -\nabla \cdot \left( -D_{s,k} \left( \nabla c_{s,k} - \frac{\Omega c_{s,k}}{RT} \nabla \sigma_{h,k} \right) \right) \quad (26)$$

Substitute Eqs. (14) into (26) and expand in the spherical coordinates yields the modified diffusion equations:

$$\begin{aligned} \frac{\partial c_{s,k}}{\partial t} &= D_{s,k} \left[ \frac{\partial^2 c_{s,k}}{\partial r^2} + \frac{2}{r} \frac{\partial c_{s,k}}{\partial r} + Z_3 \left( \frac{\partial c_{s,k}}{\partial r} \right)^2 \right. \\ &\quad \left. + Z_3 c_k \left( \frac{\partial^2 c_{s,k}}{\partial r^2} + \frac{2}{r} \frac{\partial c_{s,k}}{\partial r} \right) \right] \end{aligned} \quad (27)$$

with two boundary conditions as following

$$\begin{aligned} \frac{\partial c_{s,k}}{\partial r} \Big|_{(r=0)} &= 0 \\ -D_{s,k} (1 + Z_3 c_{s,k}) \frac{\partial c_{s,k}}{\partial r} \Big|_{(r=R_{0,k})} &= \frac{i_k}{F} \end{aligned} \quad (28)$$

where

$$Z_3 = \frac{2\Omega^2 E}{9RT(1-\nu)} \quad (29)$$

In this way, to estimate the stress profile in the P2D model, we only need to modify the diffusion equation in the solid phase as the Eq. (27) with the two boundary conditions in Eq. (28). When the P2D model is solved as usual without adding more variables [39–41], the stress profile can be obtained according to Eq. (13).

## 3. Results and discussion

In order to focus on analyzing the effect of the adding NCA on the LMO material, we only consider and discuss the stress generation inside the LMO particles. First, we show the simulated results for the pure LMO/Carbon cell. And then, the investigations for the cells with mixed electrode (LMO and NCA) are presented. The properties of the materials and parameters used in the following simulations are given in [Tables 1](#) and [2](#). [Fig. 2](#) shows the simulated

**Table 1**  
Properties for the active materials.

Parameters	Values		
	LMO	NCA	Carbon
$c_{\max}$ (mol m <sup>-3</sup> )	24161.23 <sup>c</sup>	49459.2 <sup>c</sup>	26,389 <sup>d</sup>
$D_s$ (m <sup>2</sup> s <sup>-1</sup> )	1.0e <sup>-13a</sup>	See Eq. (A7) <sup>a</sup>	3.9e <sup>-14d</sup>
$k_{Li}$ (mol <sup>-0.5</sup> m <sup>2.5</sup> s <sup>-1</sup> )	5.0e <sup>-10a</sup>	1e <sup>-10a</sup>	2.334e <sup>-11c</sup>
$R_0$ (m)	1.7e <sup>-6a</sup>	2.5e <sup>-6a</sup>	12.5e <sup>-6d</sup>
$\theta^0$	0.19 <sup>c</sup>	0.412 <sup>c</sup>	0.65 <sup>c</sup>
$R_{conc}$ (Ω m <sup>2</sup> )	0.05 <sup>a</sup>	0.04 <sup>a</sup>	0 <sup>c</sup>
$E$ (GPa)	10 <sup>b</sup>	—	—
$\nu$	0.3 <sup>b</sup>	—	—
$\Omega$ (mol m <sup>-3</sup> )	2.29e <sup>4b</sup>	—	—

<sup>a</sup> Obtained from Ref. [25].

<sup>b</sup> Obtained from Ref. [28].

<sup>c</sup> Assumed.

<sup>d</sup> Obtained from Ref. [40].

results for a pure LMO/Carbon cell discharged at C/2 to 3.0 V. The 1 C-rate is given as 10.75 A m<sup>-2</sup>. Fig. 2(a) shows the distribution of the concentration of lithium ions on the surface of the particles in the cathode at selected times. As shown in Fig. 2(a), the surface concentration of particles near the separator ( $x = 1$ ) is higher than that of the other particles. This indicates that the Li ion insertion is not homogeneous along the positive electrode and more Li ions are inserted into the particles near the separator.

Fig. 2(b) shows the distribution of the maximum radial stress in the particles in the positive electrode at the same selected times as in Fig. 2(a). The maximum radial stress is the largest radial stress inside a particle at the given time. The stress profiles presented in Fig. 2(b) show different trends compared to the surface SOC distribution presented in Fig. 2(a). The stress in the particles near the separator is not always the largest stress. This is different from that of the LiCoO<sub>2</sub> cathode as reported by Renganathan et al. [33].

It should be noted that the maximum radial stress is located at the center of the particle. This can be verified as follows. Taking the derivative of the radial stress shown in Eq. (12) with respect to  $r$  yields:

$$\frac{d\sigma_r}{dr} = \frac{2QE}{3(1-\nu)} \left( -\frac{\int_0^r \frac{dc}{dr} r^3 d\zeta}{r^4} \right) \quad (30)$$

**Table 2**  
Model parameters.

Parameters	Values		
	Positive	Separator	Negative
$\varepsilon_1$	0.4166 <sup>a</sup>	—	0.428 <sup>b</sup>
$\varepsilon_2$	0.4 <sup>a</sup>	0.37 <sup>a</sup>	0.4 <sup>a</sup>
$L$ (m)	50e <sup>-6a</sup>	50e <sup>-6a</sup>	70e <sup>-6b</sup>
$\sigma$ (S m <sup>-1</sup> )	10 <sup>a</sup>	—	100 <sup>c</sup>
$\tau$	2.89 <sup>a</sup>	3.15 <sup>a</sup>	2.5 <sup>b</sup>
$\alpha_a$	0.5 <sup>b</sup>	—	—
$\alpha_c$	0.5 <sup>b</sup>	—	—
$t^+$	0.363 <sup>a</sup>	—	—
$c_{Li}^0$ (mol m <sup>-3</sup> )	1000 <sup>a</sup>	—	—
$D$ (m <sup>2</sup> s <sup>-1</sup> )	See Eq. (A3) <sup>a</sup>	—	—
$\kappa$ (mol m <sup>-3</sup> )	See Eq. (A4) <sup>a</sup>	—	—
$F$ (C equiv <sup>-1</sup> )	96,487	—	—
$R$ (J mol <sup>-1</sup> K <sup>-1</sup> )	8.314	—	—
$T$ (K)	298.15	—	—

<sup>a</sup> Obtained from Ref. [25].

<sup>b</sup> Assumed.

<sup>c</sup> Obtained from Ref. [40].

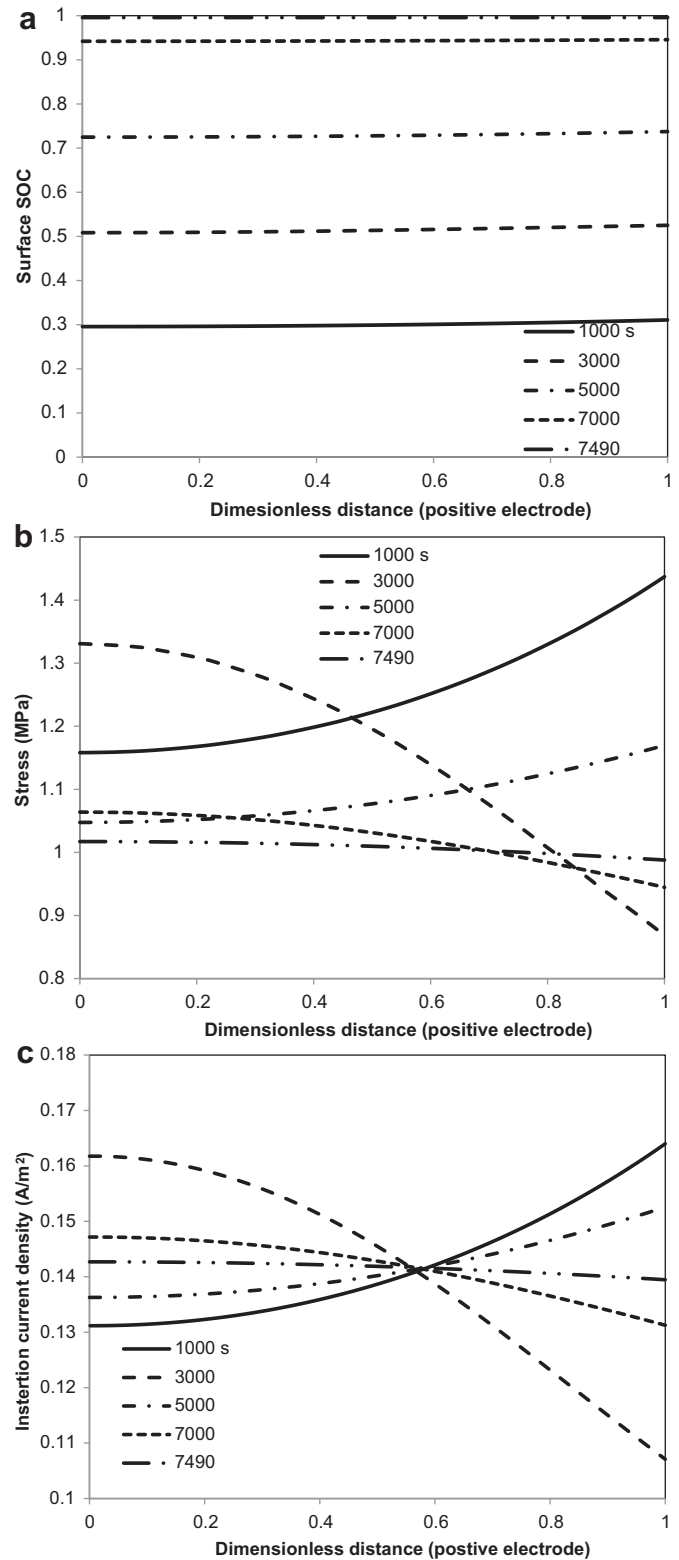


**Fig. 2.** Simulated Li insertion into LMO particle in a pure LMO/carbon cell discharged at C/2 to 3.0 V. (a) Surface state of charge; (b) maximum radial stresses; (c) insertion current density in the LMO particle across thickness of cathode at selected time ( $t = 1000, 3000, 5000, 7000, 7500$  s).



Since  $dc/dr > 0$  during Li insertion, then  $d\sigma_r/dr$  is less than zero in the particle. It means that the maximum radial stress in a particle is located at the center and according to Eq. (13) it is given by

$$\sigma_{r,\max} = \frac{2QE}{9(1-\nu)} \left[ \frac{3}{R_0^3} \int_0^{R_0} cr^2 dr - c \right]_{r=0} \quad (31)$$

The two terms within the bracket in Eq. (31) are the average concentration and the concentration at the center of the particle, respectively. During discharge (Li insertion into the positive electrode particles), the concentration at the center of the particle is the lowest, that is, the average concentration is greater than the central concentration. The maximum radial stress obtained from Eq. (31) in a particle is a positive value, which means that the radial stress is a tensile stress during Li insertion. Inversely, during charge, the radial stress is negative and minimum (maximum in the absolute value) at the center of the particle. That is, the radial stress within the particle is a compressive stress and the maximum compressive radial stress is at the center of particle. In the following discussion, the maximum radial stress is the absolute value of the maximum (in magnitude) radial stress inside particle. It should be kept in mind that the radial stress is a tensile stress during Li insertion and is a comprehensive stress during Li extraction.

The maximum and minimum tangential stresses can be obtained as follows. Taking the derivative of the tangential stress shown in Eq. (12) with respect to  $r$  yields:

$$\frac{d\sigma_t}{dr} = \frac{QE}{3(1-\nu)} \left( -\frac{3 \frac{dc}{dr} r^4 + \int_0^r \frac{dc}{dr} r^4 d\zeta}{4r^4} \right) \quad (32)$$

Since  $dc/dr > 0$  during Li insertion,  $d\sigma_t/dr$  is less than zero. Therefore, the maximum tangential stress in a particle is located at the center ( $r = 0$ ) and the minimum tangential stress is located at the particle surface ( $r = R_0$ ). The maximum and the minimum tangential stresses are given as follows:

$$\begin{aligned} \sigma_{t,\max} &= \frac{2QE}{9(1-\nu)} \left[ \frac{3}{R_0^3} \int_0^{R_0} cr^2 dr - c \right]_{r=0} \\ \sigma_{t,\min} &= \frac{QE}{3(1-\nu)} \left[ \frac{3}{R_0^3} \int_0^{R_0} cr^2 dr - c \right]_{r=R_0} \end{aligned} \quad (33)$$

By comparing Eqs. (31) and (33), we can see that the maximum tangential stress is equal to the maximum radial stress and both are tensile stresses during the discharging process, similar to the numerical results reported in the literature [27]. The minimum tangential stress is less than zero during discharge, because that the concentration of Li ions on the particle surface is greater than elsewhere within the particle. Since the minimum tangential stress is negative, it is the maximum compressive stress during discharge. If the stress-driven diffusion is ignored in the diffusion equation, the analytic solution for the concentration distribution in a spherical particle can be obtained as follows: [42].

$$\begin{aligned} c_{s,k}(r, t) &= c_{s,p,\text{avg}}(t) - \frac{i_k R_{0,k}}{FD_{s,k}} \left[ \frac{1}{2} \left( \frac{r}{R_{0,k}} \right)^2 - \frac{3}{10} \right. \\ &\quad \left. - 2 \frac{R_{0,k}}{r} \sum_{n=1}^{\infty} \frac{\sin\left(\frac{\lambda_n r}{R_{0,k}}\right)}{\lambda_n^2 \sin(\lambda_n)} \exp\left(\frac{-D_{s,k} \lambda_n^2 t}{R_{0,k}^2}\right) \right] \end{aligned} \quad (34)$$

where the average concentration  $c_{s,p,\text{avg}}(t) = (3/R_0^3) \int_0^{R_0} cr^2 dr$  and the Eigenvalue  $\lambda_n$  can be obtained by solving the Eigen equation:  $\tan(\lambda_n) = \lambda_n$ . The difference between the average concentration and the central concentration can be obtained from Eq. (34) as follows:

$$\begin{aligned} c_{s,p,\text{avg}}(t) - c|_{r=0} &= \frac{i_k R_{0,k}}{FD_{s,k}} \left( -\frac{3}{10} - 2 \sum_{n=1}^{\infty} \frac{1}{\lambda_n^2 \sin(\lambda_n)} \right. \\ &\quad \left. \times \exp\left(\frac{-D_{s,k} \lambda_n^2 t}{R_{0,k}^2}\right) \right) \end{aligned} \quad (35)$$

The difference between the average concentration and the surface concentration is given by:

$$c_{s,p,\text{avg}}(t) - c|_{r=R_0} = \frac{i_k R_{0,k}}{FD_{s,k}} \left( \frac{2}{10} - 2 \sum_{n=1}^{\infty} \frac{1}{\lambda_n^2} \exp\left(\frac{-D_{s,k} \lambda_n^2 t}{R_{0,k}^2}\right) \right) \quad (36)$$

Substitution Eqs. (35) and (36) into (33), we have:

$$\begin{aligned} \text{abs}(\sigma_{t,\max}) - \text{abs}(\sigma_{t,\min}) &= -\frac{2QE}{9(1-\nu)} \frac{i_k R_{0,k}}{FD_{s,k}} \\ &\quad \sum_{n=1}^{\infty} \left( \frac{2}{\lambda_n \sin(\lambda_n)} + \frac{3}{\lambda_n^2} \right) \exp\left(\frac{-D_{s,k} \lambda_n^2 t}{R_{0,k}^2}\right) < 0 \end{aligned} \quad (37)$$

Because  $i_k$  is less than zero during discharge, and  $\sum_{n=1}^{\infty} (2/\lambda_n \sin(\lambda_n) + 3/\lambda_n^2) \exp(-D_{s,k} \lambda_n^2 t/R_{0,k}^2)$  is less than zero, so Eq. (37) is less than zero. Eq. (37) shows that the maximum compressive tangential stress ( $\sigma_{t,\min}$ ) is greater than the maximum tensile radial/tangential stress ( $\sigma_{t,\max}/\sigma_{r,\max}$ ) during discharge. But, the difference shown in Eq. (37) becomes negligible, when the concentration gradient is well developed ( $t > (R_{0,k}^2/D_{s,k})$ ). This is similar to the numerical results reported by Christensen et al. [27] Cheng et al. have also derived that the steady value of these two maximum stresses are the same if distribution of insertion current density and stress-driven diffusion are neglected.

The distributions of the insertion current density for LMO in the positive electrode ( $i_{\text{LMO}}$ ) at the selected time were presented in Fig. 2(c). Fig. 2(b) and (c) show that the distributions of maximum radial stress and the insertion current density for LMO have the same patterns. For example, at  $t = 1000$  s, both the radial stress and the transfer current for LMO near the separator are maximum in the cathode. Moreover, it can be found that the maximum radial stress is almost proportional to the insertion current density at each point in the cathode. The same phenomena were found in the stress studies with a single particle model [26,27] where the maximum stress inside a particle almost linearly increases with the insertion current density.

Fig. 3 shows the maximum radial stresses in LMO particles in a pure LMO electrode vs. time at the interface between the cathode and the separator (Sep) and the interface between the current collector and the cathode (CC) during a C/2 discharge. The results

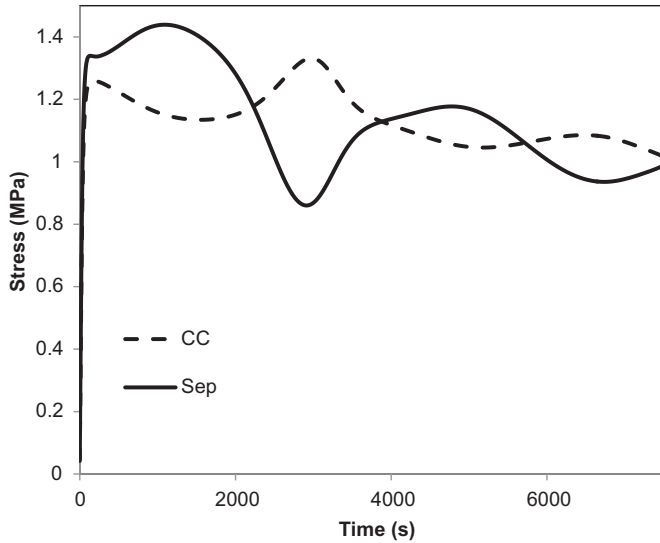


**Fig. 3.** Maximum radial stress vs. time for LMO particles at different positions: current collector (dash line) and separator (solid line) in a pure LMO electrode discharged at C/2 to 3.0 V.

indicate that although the stress in the particle at the interface between the cathode and the separator is not always the largest during the C/2 discharge, the largest insertion stress (around 1000 s) occurs at this interface. Since the particle fracture is more related to the largest tensile stress the particle has suffered, therefore, the fracture and loss integrity occur more likely in the particles near the separator [34]. The fluctuation of the stress profile on a given position shown in Fig. 3 is similar to Figure 1 in Ref. [28] and Figure 6 in Ref. [34]. As discussed earlier, this stress distribution is due to the change of insertion current density on the particle surface over time.

Fig. 4 shows the maximum radial stresses as functions of applied current obtained from two different models: a single particle model and a P2D model. The maximum radial stresses here are referred to maximum radial stress in the whole electrode during the discharge process at a given applied current,  $I_{app}$ . In the single particle model, the distribution of the insertion current density is ignored due to

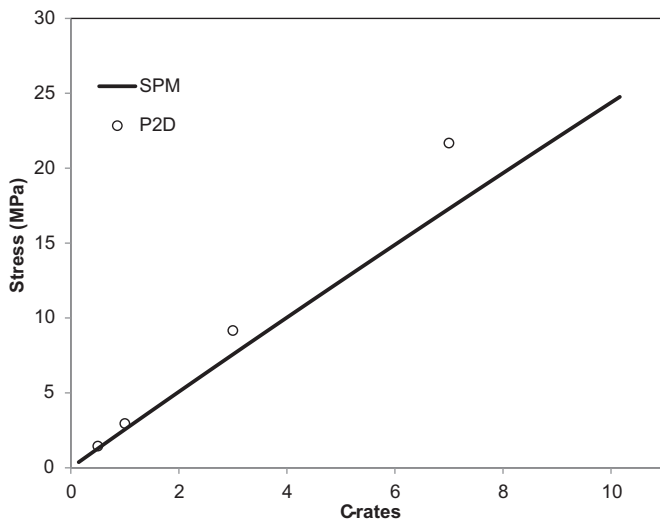


**Fig. 4.** Maximum radial stress vs. C-rates calculated with two different models: porous electrode model (circle) and single particle model (solid line).

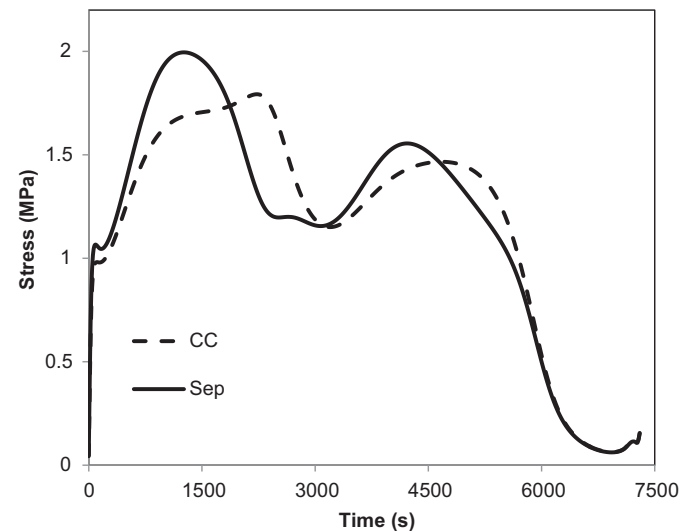
the assumptions of the constant electrolyte concentration and the constant solution phase potential in the cell. In the single particle model, we only solve the Eq. (27) with two boundary conditions in Eq. (28). The insertion current density  $i_k$  on the particle surface is given by:

$$i_k = \frac{I_{app} R_{0,LMO}}{3\epsilon_{1,LMO} l_p} \quad (38)$$

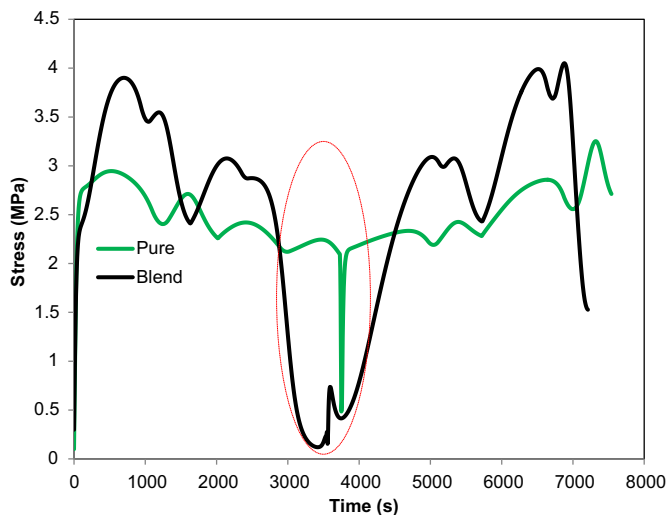
The stress profile is calculated based on the Eq. (13). As shown in Fig. 4, the simulated maximum radial stress obtained from a P2D model is higher than that obtained from a single particle model, especially at the high C-rates. This is because the non-uniform distribution in the transfer current in the cathode is considered in a P2D model as discussed above. It is indicated that the concentration and potential gradient in the solution phase plays an important role in the mechanical behavior of a cell. Also, the electrode design parameters, such as: the porosity and the thickness, which affect the transport of Li ions in the solution, need to be carefully chosen based on the application of the cell. The effects of these parameters on the cell's mechanical behavior have been investigated in our previous work [33].

Fig. 5 shows the simulated maximum radial stress for LMO particles at selected positions (CC: near the current collector; Sep: near the separator) in a mixed electrode (LMO:NCA = 0.67:0.33, volume fraction) which is discharged at C/2 to 3 V. Although the cell capacity increases by increasing the fraction of NCA in the electrode, the 1 C-rate current for all mixed electrodes in this study is given as the same value in the pure LMO cell, which is  $10.75 \text{ A m}^{-2}$ . The stress profiles shown in Fig. 5 for the LMO particles in a mixed electrode are similar to those shown in Fig. 3 for a pure LMO electrode during a C/2 discharge expect for the end part of discharge (time is greater than 5500 s). As shown in Fig. 5, at the end part of discharge, the stress in the LMO particles is reduced significantly. This is because during the end part of discharge, most Li ions are inserted into the NCA particles due to the OCP difference between LMO and NCA. As shown in Fig. A-1 in the Appendix, the open circuit potential of NCA in the discharged state is much lower than that of LMO.

Fig. 6 shows the simulated maximum stresses in a pure LMO cathode and a mixed cathode (LMO:NCA = 0.67:0.33, volume



**Fig. 5.** Stress profile of LMO particle at different position: current collector (dash line) and separator (solid line) in mixed electrode (LMO:NCA = 0.67:0.33, volume fraction) with C/2 discharged to 3.0 V.



**Fig. 6.** Maximum radial stress inside LMO particle vs. time with 1 C discharge/charge cycling of mixed electrode (black, LMO:NCA = 0.67:0.33, volume fraction) or pure electrode (green)/carbon full cell between 3.0 V and 4.3 V. The ellipse indicated the stress reduction region in the mixed electrode compared to pure electrode during cycling. (For interpretation of the references to colour in this figure legend, the reader is referred to the web version of this article.)

fraction) as functions of time during a 1 C discharge/charge cycle. The black line represents the stress profile obtained from a blended material cathode; the green (in web version) line is maximum stress profile for the pure LMO cathode. As shown in Fig. 6 (red ellipse (in web version)), the stress of LMO particle in the discharged state is reduced due to mixed with the NCA particles compared that obtained from a cell with a pure LMO cathode.

Some experimental work has shown that the dissolution of Mn from spinel LMO is a serious process in a discharged state during cell cycling [43–45]. Mn dissolution into the electrolyte due to acid attack and a disproportionation reaction at the particle surface is most likely to happen with more  $\text{Mn}^{3+}$  inside particle when the cell is in the discharged state. If there is a protective layer on the particle surface such as a coating layer or a SEI layer, the Mn dissolution can

be reduced [9]. As determined by experiments, the inactive layer is always formed on the LMO particle surface due to the Mn dissolution and the electrolyte oxidation [46,47]. However, unlike the bulk LMO particles which have been treated at high temperature, the newly formed layer may be weak and be easily destroyed due to the stress as shown in Fig. 7. Therefore, the decrease in the stress in the discharged state for LMO particles in the mixed cathode may suppress the fracture of the SEI layer. Therefore, the existence of the layer in the discharge state can effectively protect the LMO surface from the acid attack and reduce the Mn dissolution. Moreover, if the stress on the particle surface contributed to the Mn dissolution directly due to the increase of strain energy, the Mn dissolution would be suppressed when the stress is reduced. As discussed above, the reduction of the stress in a discharged state can explain the experimental observations that the performance of LMO based electrode are improved by adding NCA [16].

The maximum radial stress of the cell with mixed electrode (LMO:NCA = 0.67:0.33, volume fraction) during a constant current discharge/charge cycles (CC–CC protocol) at 1 C is shown in Fig. 8. The results indicate that the stresses in the latter cycles are similar to that in the first cycle in this study. This is because the current is low, the effect of previous Li insertion and extraction on the stress vanishes within a short timescale [27]. The maximum radial stress in a cell cycled with the CC discharge–CC charge protocol is presented in Fig. 9. This protocol consists of a constant current discharge at 1 C to 3.0 V, followed by a constant current charge at 1 C to a selected cutoff charge voltage, and then a constant voltage charge until the current drops to the cutoff current. Similarly to the CC–CC protocol cycle, there is no stress accumulation during the cell cycling in this study. Also, the simulation shows that the stress generation during the CV charge with a cutoff voltage of 4.3 V is similar to that with a cutoff voltage of 4.2 V. The simulated maximum stress profiles for the mixed LMO and NCA electrodes with four different volume ratios are shown in Fig. 10. The following volume ratios between LMO and NCA are selected in this study: LMO:NCA = 0.9:0.1, 0.67:0.33, 0.5:0.5, 0.33:0.67. The cells are discharged at 3 C to 3.0 V. As expected, the reduced stress region increases with increasing the volume fraction of NCA. But it is also observed from Fig. 10 that the maximum stress during discharge (as indicated by the dash arrow) increases by adding more NCA into the mixed electrode. Therefore, the tradeoff between the decrease in

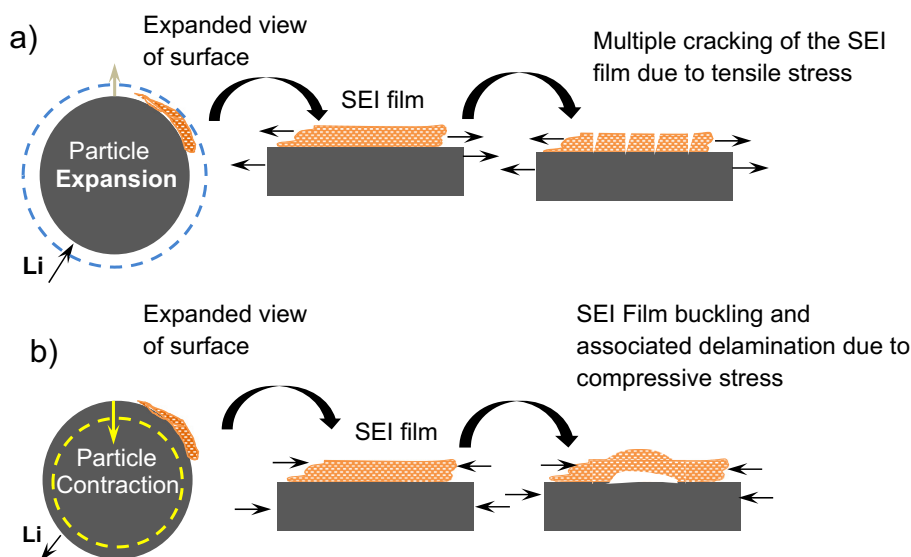


**Fig. 7.** Schematic of failure that may occur in LMO particle surface due to Li insertion/extraction: (a) Li insertion (discharge); (b) Li extraction (charge).



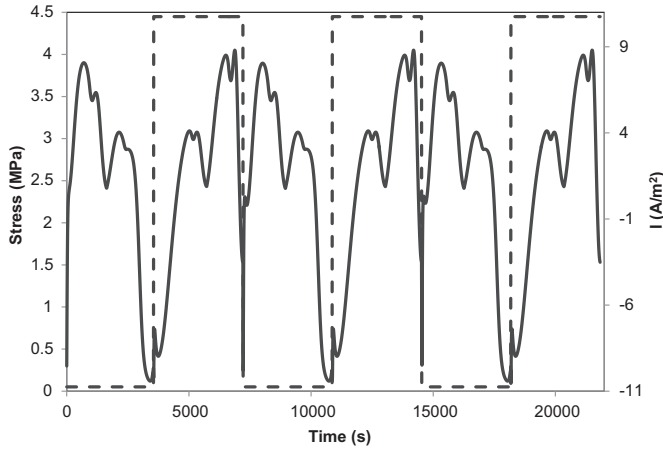


**Fig. 8.** Simulated stress generation inside LMO particle with 1 C discharge/charge cycling of mixed electrode (LMO:NCA = 0.67:0.33, volume fraction) between 3.0 V and 4.3 V. The dash line is the applied current, corresponding to right axis. Positive current is charged process, and negative current is discharged process.

the stress in the end part of discharge and the increase in the maximum stress has to be considered when determining the volume fraction of NCA in the mixed electrode.

#### 4. Conclusions

A mathematical model is developed in this study to understand the stress generation inside the LMO particle during discharge/charge in a Li-ion battery with a pure LMO or a mixed electrode (LMO and NCA) cathode. Simulation results for the pure LMO/carbon full cell show that the stress generation inside LMO particle is non-uniform within the positive electrode. The results also indicate that the fracture or loss of particle integrity potentially occurs in the particles near the separator. The stress profiles obtained from a single particle model and a porous electrode model show a significant difference for the high C rate discharge. This indicates that the single particle model cannot be used because of the non-

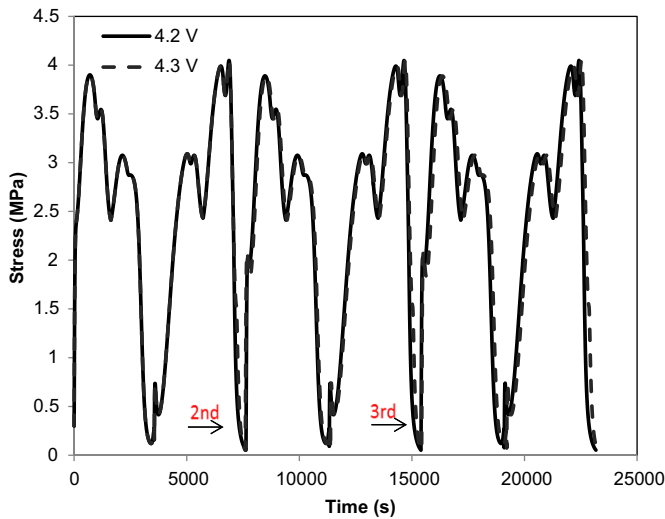


**Fig. 9.** Simulated stress generation inside LMO particle in mixed electrode (LMO:NCA = 0.67:0.33, volume fraction) with 1 C discharge/1 C charge to cut-off voltage and constant current charge to cut-off current. Two different cut-off charge voltages, 4.2 V (solid line) and 4.3 V (dash line) are applied. The arrow in the picture indicates a new cycle.

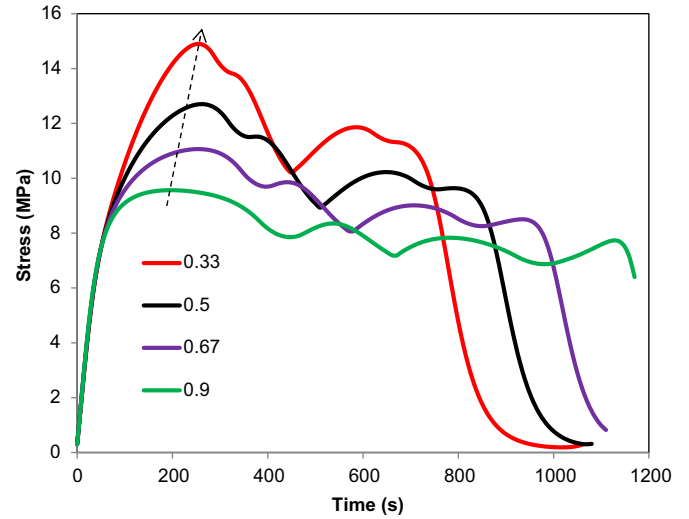


**Fig. 10.** Simulation stress vs. time, of different blend ratio mixed electrode with 3 C discharged to 3.0 V. 0.33 – red, 0.5 – black, 0.67 – purple, 0.9 – green of LMO volume fraction in mixed electrode. The dash arrow indicates the largest stress during the whole discharge process. (For interpretation of the references to colour in this figure legend, the reader is referred to the web version of this article.)

uniform distributions in the concentration and the potential in the electrolyte in the high current rate studies. Simulation results for a mixed electrode show that the stress generated in the LMO particles is significantly reduced at the end of discharge in a mixed LMO and NCA electrode due to the OCP difference between the LMO and NCA. This stress reduction might partially explain why experiment investigations show that the performance of the LMO based electrodes can be improved by adding NCA. Simulations for mixed electrodes with different blend ratios show that the reduced stress region increases by increasing the NCA ratio.

#### Appendix

The effective ionic conductivity and diffusion coefficient in the binary electrolyte are determined by the following equations, respectively: [36].

$$\kappa_{\text{eff},j} = \frac{\kappa \varepsilon_{2,j}}{\tau_j}, \quad j = p, s, n \quad (\text{A1})$$

$$D_{\text{eff},j} = \frac{D \varepsilon_{2,j}}{\tau_j}, \quad j = p, s, n \quad (\text{A2})$$

where  $\tau_j$  is the tortuosity of the porous electrode.

The concentration dependent ionic conductivity and the diffusion coefficient in the binary electrolyte are given by: [36].

$$\kappa = 0.84 \left( \frac{1.134 \frac{c_{\text{Li}^+}}{1000}}{1 + 0.2 \left( \frac{c_{\text{Li}^+}}{1000} \right) + 0.08 \left( \frac{c_{\text{Li}^+}}{1000} \right)^4} + 0.1 \right) \quad (\text{A3})$$

$$D = 6.5 \times 10^{-10} \exp \left( -0.7 \frac{c_{\text{Li}^+}}{1000} \right) \quad (\text{A4})$$

The effective conductivity in the solid phase is defined as

$$\sigma_{\text{eff},j} = \sigma_j, \quad j = p, n \quad (\text{A5})$$

The ionic activity coefficient,  $f$ , is given as following: [36].

$$1 + \frac{\partial \ln f}{\partial \ln c_{\text{Li}^+}} = 1 + \frac{c_{\text{Li}^+}}{1000} \left[ \frac{-1.0178}{2 \left( 1 + 0.9831 \left( \frac{c_{\text{Li}^+}}{1000} \right)^{0.5} \right)} \right. \\ \left. \times \left( \frac{1}{\left( \frac{c_{\text{Li}^+}}{1000} \right)^{0.5}} - \frac{0.9831}{1 + 0.9831 \left( \frac{c_{\text{Li}^+}}{1000} \right)^{0.5}} \right) + 1.5842 \right] \quad (\text{A6})$$

The Li diffusion coefficient in NCA particle [36] is given as follows:

$$D_{s,\text{NCA}} = 3 \times 10^{-15} ((1 + \tan h(-20(\theta_{\text{NCA}} - 0.73))) + 0.02) \quad (\text{A7})$$

The open circuit potentials for the  $\text{LiMn}_2\text{O}_4$  cathode as functions of state of charge are given by: [48].

$$U_{\text{LMO}} = 4.199 + 0.05661 \tan h(-14.555\theta_{\text{LMO}} + 8.609) \\ - 0.0275 \left( \frac{1}{(0.998 - \theta_{\text{LMO}})^{0.492}} - 1.901 \right) \\ - 0.157 \exp(-0.0474\theta_{\text{LMO}}^8) \\ + 0.810 \exp(-40(\theta_{\text{LMO}} - 0.134)). \quad (\text{A8})$$

The open circuit potential for NCA (fit to experimental data) is given by:

$$0.36 \leq \theta_{\text{NCA}} \leq 0.410,$$

$$U_{\text{NCA}} = 8.535 - 17.059\theta_{\text{NCA}} + 21.038\theta_{\text{NCA}}^2 - 9.153\theta_{\text{NCA}}^3 \\ + 9.875(\theta_{\text{NCA}} - 0.700)^3 - 2.176(\theta_{\text{NCA}} - 0.550)^3 \\ - 1331.866(\theta_{\text{NCA}} - 0.410)^3; \quad (\text{A9})$$

$$0.410 \leq \theta_{\text{NCA}} \leq 0.55,$$

$$U_{\text{NCA}} = 8.535 - 17.059\theta_{\text{NCA}} + 21.038\theta_{\text{NCA}}^2 - 9.153\theta_{\text{NCA}}^3 \\ + 9.875(\theta_{\text{NCA}} - 0.700)^3 - 2.176(\theta_{\text{NCA}} - 0.550)^3; \quad (\text{A10})$$

$$0.55 \leq \theta_{\text{NCA}} \leq 0.7,$$

$$U_{\text{NCA}} = 8.535 - 17.059\theta_{\text{NCA}} + 21.038\theta_{\text{NCA}}^2 - 9.153\theta_{\text{NCA}}^3 \\ + 9.875(\theta_{\text{NCA}} - 0.700)^3; \quad (\text{A11})$$

$$0.7 \leq \theta_{\text{NCA}} \leq 0.935,$$

$$U_{\text{NCA}} = 8.535 - 17.059\theta_{\text{NCA}} + 21.038\theta_{\text{NCA}}^2 - 9.153\theta_{\text{NCA}}^3; \quad (\text{A12})$$

$$0.935 \leq \theta_{\text{NCA}} \leq 0.959,$$

$$U_{\text{NCA}} = 8.535 - 17.059\theta_{\text{NCA}} + 21.038\theta_{\text{NCA}}^2 - 9.153\theta_{\text{NCA}}^3 \\ + 9.875(\theta_{\text{NCA}} - 0.700)^3 - 5370.872(\theta_{\text{NCA}} - 0.935)^3; \quad (\text{A13})$$

$$0.959 \leq \theta_{\text{NCA}} \leq 0.980,$$

$$U_{\text{NCA}} = 8.535 - 17.059\theta_{\text{NCA}} + 21.038\theta_{\text{NCA}}^2 - 9.153\theta_{\text{NCA}}^3 \\ + 9.875(\theta_{\text{NCA}} - 0.700)^3 - 5370.872(\theta_{\text{NCA}} - 0.935)^3 \\ - 47690.304(\theta_{\text{NCA}} - 0.959)^3. \quad (\text{A14})$$

And the open circuit potential for the carbon anode (fit to experimental data) is as follows:

$$0.001 \leq \theta_{\text{C}} \leq 0.0109,$$

$$U_{\text{C}} = 0.113 - 0.0208 \tan h(15.064\theta_{\text{C}} - 8.199) \\ - 2.435(\theta_{\text{C}} - 0.440)^3 + 65.394(\theta_{\text{C}} - 0.154)^3 \\ - 960.307(\theta_{\text{C}} - 0.0897)^3 - 1.006 \times 10^7(\theta_{\text{C}} - 0.0109)^3; \quad (\text{A15})$$

$$0.0109 \leq \theta_{\text{C}} \leq 0.0897,$$

$$U_{\text{C}} = 0.113 - 0.0208 \tan h(15.064\theta_{\text{C}} - 8.199) \\ - 2.435(\theta_{\text{C}} - 0.440)^3 + 65.394(\theta_{\text{C}} - 0.154)^3 \\ - 960.307(\theta_{\text{C}} - 0.0897)^3; \quad (\text{A16})$$

$$0.0897 \leq \theta_{\text{C}} \leq 0.154,$$

$$U_{\text{C}} = 0.113 - 0.0208 \tan h(15.064\theta_{\text{C}} - 8.199) \\ - 2.435(\theta_{\text{C}} - 0.440)^3 + 65.394(\theta_{\text{C}} - 0.154)^3; \quad (\text{A17})$$

$$0.0897 \leq \theta_{\text{C}} \leq 0.154,$$

$$U_{\text{C}} = 0.113 - 0.0208 \tan h(15.064\theta_{\text{C}} - 8.199) \\ - 2.435(\theta_{\text{C}} - 0.440)^3 + 65.394(\theta_{\text{C}} - 0.154)^3; \quad (\text{A18})$$

$$0.154 \leq \theta_{\text{C}} \leq 0.440,$$

$$U_{\text{C}} = 0.113 - 0.0208 \tan h(15.064\theta_{\text{C}} - 8.199) \\ - 2.435(\theta_{\text{C}} - 0.440)^3; \quad (\text{A19})$$

$$0.440 \leq \theta_{\text{C}} \leq 0.854,$$

$$U_{\text{C}} = 0.113 - 0.0208 \tan h(15.064\theta_{\text{C}} - 8.199); \quad (\text{A20})$$

$$0.854 \leq \theta_{\text{C}} \leq 0.92,$$

$$U_{\text{C}} = 0.113 - 0.0208 \tan h(15.064\theta_{\text{C}} - 8.199) \\ - 252.707(\theta_{\text{C}} - 0.854)^3; \quad (\text{A21})$$

where the SOC,  $\theta$ , is defined by:

$$\theta_k = \frac{c_{\text{surf},k}}{c_{\text{max},k}}, \quad k = \text{LMO, NCA, C} \quad (\text{A22})$$

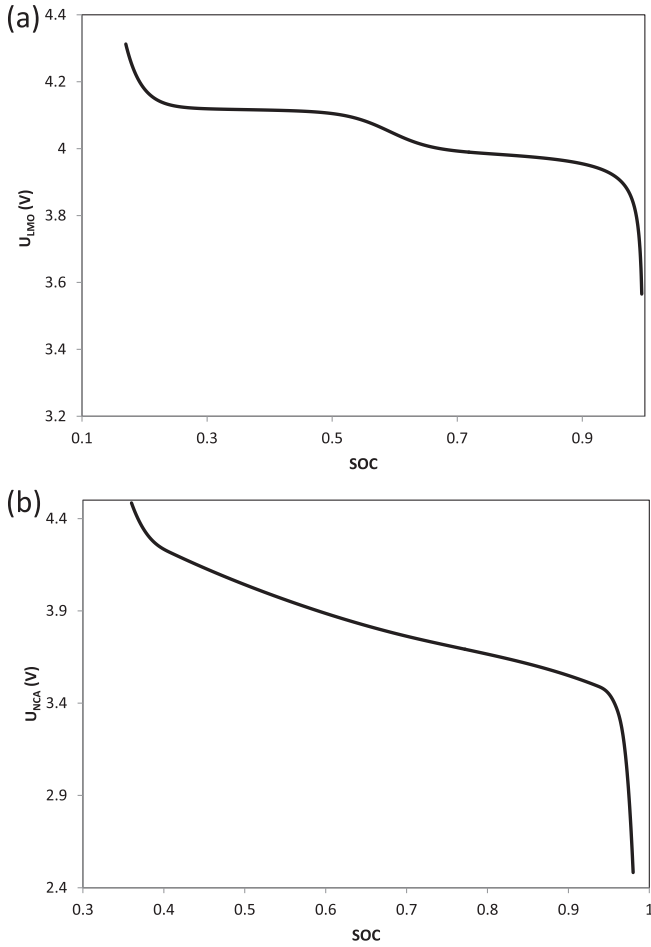


Fig. A-1. The open circuit potential profiles for (a) LMO; (b) NCA.

## List of symbols

$a_k$	specific surface area of particle type $k$ , $\text{m}^2 \text{m}^{-3}$
$\text{brugg}_j$	Bruggeman coefficient in region $j$ ( $j = n, s, p$ )
$c_{\text{Li}^+}$	concentration of $\text{Li}^+$ in the solution phase, $\text{mol m}^{-3}$
$c_{s,k}$	concentration of lithium ions in the particle type $k$ , $\text{mol m}^{-3}$
$c_{s,k}^0$	initial concentration of lithium ions in the particle type $k$ , $\text{mol m}^{-3}$
$c_{s,\text{max},k}$	maximum concentration of lithium ions in the particle type $k$ , $\text{mol m}^{-3}$
$\Delta c_s$	concentration change from initial value, $\text{mol m}^{-3}$
$D$	$\text{Li}^+$ diffusion coefficient in the electrolyte, $\text{m}^2 \text{s}^{-1}$
$D_{s,k}$	lithium ion diffusion coefficient in the particle type $k$ , $\text{m}^2 \text{s}^{-1}$
$E$	Young's modulus, GPa
$f$	ionic activity coefficient
$F$	Faraday's constant, $96,487 \text{ C equiv}^{-1}$
$I_{\text{app}}$	applied current density, $\text{A m}^{-2}$

$i_{0,k}$	exchange current density, $\text{A m}^{-2}$
$i_k$	transfer current on the surface of particle type $k$ , $\text{A m}^{-2}$
$I_j$	total current density, $\text{A m}^{-3}$
$k_{\text{Li},k}$	Li intercalation/deintercalation reaction rate constant for particle type $k$ , $\text{A m}^{2.5} \text{mol}^{-1.5}$
$L_p$	thickness of positive electrode, m
$L_s$	thickness of separator, m
$L_n$	thickness of negative electrode, m
$n$	negative electrode
$p$	positive electrode
$r$	radial coordinate, m
$R$	universal gas constant, $\text{J mol}^{-1} \text{K}^{-1}$
$R_{0,k}$	radius of the particle type $k$ , m
$R_{\text{conc}}$	contact resistance on the surface of particle type $k$ , $\Omega \text{ m}^2$
$s$	separator
$t$	time, s
$t^+$	$\text{Li}^+$ transference number in the electrolyte
$T$	environment temperature, K
$\Delta T$	temperature change from initial value, K
$u$	displacement, m
$U_k$	equilibrium potential of Li interaction/deinteraction reaction for particle type $k$ , V
$x$	spatial coordinate, m
$Z_1, Z_2$	integration constant

## Greek letters

$\alpha$	thermal expansion coefficient
$\alpha_a$	anodic transfer coefficient
$\alpha_c$	cathodic transfer coefficient
$\varepsilon_{1,k}$	volume fraction of the particle type $k$ in the electrode
$\varepsilon_{2,j}$	porosity in region $j$ ( $j = n, s, p$ )
$\varepsilon_{ij}$	strain
$\theta$	dimensionless concentration of lithium ions in the particle ( $\theta = c_{s,\text{surf}}/c_{s,\text{max}}$ )
$\theta^0$	initial dimensionless concentration of lithium ions in the particle ( $\theta = c_{s,\text{surf}}/c_{s,\text{max}}$ )
$\kappa$	ionic conductivity of the electrolyte, $\text{S m}^{-1}$
$\kappa_{\text{eff}}$	effective ionic conductivity of the electrolyte, $\text{S m}^{-1}$
$\sigma$	electronic conductivity of the solid phase, $\text{S m}^{-1}$
$\sigma_{\text{eff}}$	effective electronic conductivity of the solid phase, $\text{S m}^{-1}$
$\sigma_{ij}$	stress, Pa
$\phi_1$	solid phase potential, V
$\phi_2$	solution phase potential, V
$\eta_k$	over-potential, V
$\zeta$	dummy integration variable
$\nu$	Poisson's ratio
$\delta_{ij}$	Kronecker delta
$\tau$	tortuosity
$\Omega$	partial molar volume, $\text{m}^3 \text{mol}^{-1}$

## Subscript

$h$	hydrostatic
$r$	radial direction
$t$	tangential direction
LMO	$\text{LiMn}_2\text{O}_4$
NCA	$\text{LiNi}_{0.8}\text{Co}_{0.15}\text{Al}_{0.05}\text{O}_2$
C	carbon

## References

- [1] G. Amatucci, A. Du Pasquier, A. Blyr, T. Zheng, J.M. Tarascon, *Electrochim. Acta* 45 (1999) 255.
- [2] M. Wohlfahrt-Mehrens, C. Vogler, J. Garche, *J. Power Sources* 127 (2004) 58.

- [3] W. Choi, A. Manthiram, *J. Electrochem. Soc.* 153 (2006) A1760.
- [4] S. Komaba, N. Kumagai, Y. Kataoka, *Electrochim. Acta* 47 (2002) 1229.
- [5] P. Arora, R.E. White, M. Doyle, *J. Electrochem. Soc.* 145 (1998) 3647.
- [6] D.H. Jang, Y.J. Shin, S.M. Oh, *J. Electrochem. Soc.* 143 (1996) 2204.
- [7] Y.L. Dai, L. Cai, R.E. White, *J. Electrochem. Soc.* 160 (2013) A182.
- [8] Y.Y. Xia, Y.H. Zhou, M. Yoshio, *J. Electrochem. Soc.* 144 (1997) 2593.
- [9] G.G. Amatucci, A. Blyr, C. Sigala, P. Alfonso, J.M. Tarascon, *Solid State Ionics* 104 (1997) 13.
- [10] J.M. Tarascon, W.R. Mckinnon, F. Coowar, T.N. Bowmer, G. Amatucci, D. Guyomard, *J. Electrochem. Soc.* 141 (1994) 1421.
- [11] P. Arora, B.N. Popov, R.E. White, *J. Electrochem. Soc.* 145 (1998) 807.
- [12] D. Zhang, B.N. Popov, R.E. White, *J. Power Sources* 76 (1998) 81.
- [13] G.H. Li, H. Ikuta, T. Uchida, M. Wakihara, *J. Electrochem. Soc.* 143 (1996) 178.
- [14] G.G. Amatucci, N. Pereira, T. Zheng, I. Plitz, J.M. Tarascon, *J. Power Sources* 81 (1999) 39.
- [15] W. Choi, A. Manthiram, *Electrochem. Solid State Lett.* 9 (2006) A245.
- [16] T. Numata, C. Amemiya, T. Kumeuchi, M. Shirakata, M. Yonezawa, *J. Power Sources* 97–98 (2001) 358.
- [17] S.T. Myung, M.H. Cho, H.T. Hong, T.H. Kang, C.S. Kim, *J. Power Sources* 146 (2005) 222.
- [18] H.Y. Tran, C. Taubert, M. Fleischhammer, P. Axmann, L. Kuppers, M. Wohlfahrt-Mehrens, *J. Electrochem. Soc.* 158 (2011) A556.
- [19] A. Manthiram, W. Choi, *Electrochem. Solid State Lett.* 10 (2007) A228.
- [20] A.J. Smith, S.R. Smith, T. Byrne, J.C. Burns, J.R. Dahn, *J. Electrochem. Soc.* 159 (2012) A1696.
- [21] H.F. Wang, Y.L. Jang, B.Y. Huang, D.R. Sadoway, Y.T. Chiang, *J. Electrochem. Soc.* 146 (1999) 473.
- [22] H. Gabrisch, J. Wilcox, M.M. Doeff, *Electrochem. Solid State Lett.* 11 (2008) A25.
- [23] M.R. Lim, W.I. Cho, K.B. Kim, *J. Power Sources* 92 (2001) 168.
- [24] R. Kostecki, F. McLarnon, *J. Power Sources* 119 (2003) 550.
- [25] W.I.F. David, M.M. Thackeray, L.A. Depicciotto, J.B. Goodenough, *J. Solid State Chem.* 67 (1987) 316.
- [26] R. Deshpande, M. Verbrugge, Y.T. Cheng, J. Wang, P. Liu, *J. Electrochem. Soc.* 159 (2012) A1730.
- [27] J. Christensen, J. Newman, *J. Solid State Electrochem.* 10 (2006) 293.
- [28] J. Christensen, J. Newman, *J. Electrochem. Soc.* 153 (2006) A1019.
- [29] X.C. Zhang, W. Shyy, A.M. Sastry, *J. Electrochem. Soc.* 154 (2007) A910.
- [30] Y.T. Cheng, M.W. Verbrugge, *J. Power Sources* 190 (2009) 453.
- [31] R.E. Garcia, Y.M. Chiang, W.C. Carter, P. Limthongkul, C.M. Bishop, *J. Electrochem. Soc.* 152 (2005) A255.
- [32] S. Golmon, K. Maute, M.L. Dunn, *Comput. Struct.* 87 (2009) 1567.
- [33] S. Renganathan, G. Sikha, S. Santhanagopalan, R.E. White, *J. Electrochem. Soc.* 157 (2010) A155.
- [34] J. Christensen, *J. Electrochem. Soc.* 157 (2010) A366.
- [35] A.F. Bower, P.R. Guduru, V.A. Sethuraman, *J. Mech. Phys. Solids* 59 (2011) 804.
- [36] P. Albertus, J. Christensen, J. Newman, *J. Electrochem. Soc.* 156 (2009) A606.
- [37] S.P. Timoshenko, J.N. Goodier, *Theory of Elasticity*, McGraw-Hill, New York, 1970.
- [38] F.Q. Yang, *Mat. Sci. Eng. A: Struct.* 409 (2005) 153.
- [39] M. Doyle, T.F. Fuller, J. Newman, *J. Electrochem. Soc.* 140 (1993) 1526.
- [40] T.F. Fuller, M. Doyle, J. Newman, *J. Electrochem. Soc.* 141 (1994) 1.
- [41] L. Cai, R.E. White, *J. Power Sources* 196 (2011) 5985.
- [42] V.R. Subramanian, R.E. White, *J. Power Sources* 96 (2001) 385.
- [43] M.M. Thackeray, Y. Shao-Horn, A.J. Kahaian, K.D. Kepler, J.T. Vaghey, S.A. Hackney, *Electrochem. Solid State Lett.* 1 (1998) 7.
- [44] M.C. Tucker, J.A. Reimer, E.J. Cairns, *J. Electrochem. Soc.* 149 (2002) A574.
- [45] L.F. Wang, C.C. Ou, K.A. Striebel, J.J.S. Chen, *J. Electrochem. Soc.* 150 (2003) A905.
- [46] D. Aurbach, K. Gamolsky, B. Markovsky, G. Salitra, Y. Gofer, U. Heider, R. Oesten, M. Schmidt, *J. Electrochem. Soc.* 147 (2000) 1322.
- [47] J.L. Lei, L.J. Li, R. Kostecki, R. Muller, F. McLarnon, *J. Electrochem. Soc.* 152 (2005) A774.
- [48] M. Doyle, J. Newman, A.S. Gozdz, C.N. Schmutz, J.M. Tarascon, *J. Electrochem. Soc.* 143 (1996) 1890.